NFLUX Satellite-Based Surface Radiative Heat Fluxes. Part I: Swath-Level Products

JACKIE C. MAY, CLARK ROWLEY, AND CHARLIE N. BARRON

Naval Research Laboratory, Stennis Space Center, Mississippi

(Manuscript received 18 August 2016, in final form 1 December 2016)

ABSTRACT

The Naval Research Laboratory (NRL) ocean surface flux (NFLUX) system originally provided operational near-real-time satellite-based surface state parameter and turbulent heat flux fields over the global ocean. This study extends the NFLUX system to include the production of swath-level shortwave and longwave radiative heat fluxes at the ocean surface. A companion paper presents the production of the satellite-based global gridded radiative heat flux analysis fields. The swath-level radiative heat fluxes are produced using the Rapid Radiative Transfer Model for Global Circulation Models (RRTMG), with the primary inputs of satellite-derived atmospheric temperature and moisture profiles and cloud information retrieved from the Microwave Integrated Retrieval System (MIRS). This study uses MIRS data provided for six polar-orbiting satellite platforms. Additional inputs to the RRTMG include sea surface temperature, aerosol optical depths, atmospheric gas concentrations, ocean surface albedo, and ocean surface emissivity. Swath-level shortwave flux estimates are converted into clearness index values, which are used in data assimilation because the clearness index values are less dependent on the solar zenith angle. The NFLUX swath-level shortwave flux, longwave flux, and clearness index estimates are produced for 1 May 2013–30 April 2014 and validated against observations from research vessel and moored buoy platforms. Each of the flux parameters compares well among the various satellites.

1. Introduction

The ocean surface heat budget is determined by the shortwave and longwave radiative heat fluxes and the latent and sensible turbulent heat fluxes. Accurate representation of each of these flux components is important in quantifying and understanding the heating and cooling of the ocean surface, which impacts subsurface features such as the mixed-layer and sonic-layer depths and atmospheric features such as stability and convection. Obtaining reliable surface flux measurements directly over the global ocean is challenging. In situ (ship and buoy) observations typically provide high-quality data with a long time series, but the global coverage is very sparse. Few in situ sites measure surface heat fluxes and most of these sites are located over land. An alternative to in situ observations is satellite data. Many polar-orbiting satellites with relevant measurements are currently operational and provide global coverage, with most surface locations sampled twice a day from each satellite. The drawback to using satellites is they do not measure surface fluxes directly. Instead, they provide information on flux-related atmospheric and oceanic parameters, including atmospheric temperature and moisture profiles, cloud coverage, aerosol content, and sea surface temperature (SST). These satellite-measured parameters can then be used to estimate the satellite swath-level surface heat fluxes. In an effort to give adequate attention to each of the heat flux components, only the radiative heat fluxes will be discussed in this study.

Although satellites offer an appealing alternative to in situ observations, the satellite swath-level radiative heat flux estimates typically have much larger errors than do the in situ observations because of inaccuracies in the satellite input parameters and errors in the radiative transfer model used. Some radiative transfer inputs cannot be derived from the satellite of interest and must be determined from other sources such as model analyses or forecast fields, which could add to the error in the satellite swath-level estimates. Cloud coverage causes the largest uncertainty in the downwelling shortwave radiation at the surface (SW_{dwn}; Zhang et al. 1995). Clouds, and to a lesser extent aerosols, scatter

Corresponding author e-mail: Jackie C. May, jackie.may@nrlssc.navy.mil

DOI: 10.1175/JAMC-D-16-0282.1

and reflect incoming solar radiation, reducing the amount of SW_{dwn} that reaches the surface (Trenberth et al. 2009). The largest sources of uncertainty in downwelling longwave radiation at the surface (LW_{dwn}) are atmospheric temperature and moisture, particularly in the lower levels of the atmosphere (Zhang et al. 1995, 2006). An increase in low-level atmospheric temperature or moisture increases the longwave emission from the atmosphere, thereby increasing the LW_{dwn}. Clouds, which absorb and reemit longwave radiation back to the surface, have little impact on LW_{dwn} except in high-latitude regions. Because of the multiple sources of uncertainty in the satellite swath-level estimates, they must be validated using the more robust, albeit sparser, in situ observations to provide uncertainty estimates for their use in other applications.

In comparison with the numerous studies on turbulent heat fluxes (Jourdan and Gautier 1995; Zeng et al. 1998; Yu and Weller 2007; Wang et al. 2013; May et al. 2016), studies on the radiative heat fluxes, particularly at the swath level, are rather limited. Few other satellite-based swath-level surface radiative flux datasets exist, including the Clouds and the Earth's Radiant Energy System (CERES; Kratz et al. 2010) and the Fast Longwave and Shortwave Radiative Flux (FLASHFlux; Kratz et al. 2014). Both of these products use satellite-measured top-of-atmosphere radiances along with ancillary meteorological data and cloud information to derive the surface radiative fluxes. CERES provides surface fluxes at least 6 months after the actual satellite overpass. FLASHFlux, which is based on the CERES processing, provides a rapid release version of the CERES surface fluxes within 1 week of the satellite overpass.

While the existing products provide climate-quality radiative fluxes, the temporal latency is still too great to be used in near-real-time operational applications, such as short-term ocean model forecasting. This led to the development of the Naval Research Laboratory (NRL) ocean surface flux (NFLUX) system. NFLUX is a complete data processing and assimilation system used to provide near-real-time (within hours of the satellite measurements becoming available) swath-level and gridded surface heat flux products over the global ocean. This study focuses on the production and validation of the near-real-time satellite swath-level estimates for the radiative heat fluxes. A companion paper (May et al. 2017) will discuss the production and validation of the near-real-time global gridded surface radiative flux products. For details and discussion on near-real-time satellite-based state parameters and turbulent heat fluxes within NFLUX, refer to Van de Voorde et al. (2015) and May et al. (2016).

A description of how the satellite swath-level surface radiative fluxes are calculated, including a presentation of the radiative transfer model and its major inputs, is given in section 2. Section 3 discusses the clearness index parameter. Section 4 describes the in situ data that are used to validate the swath-level estimates. The NFLUX swath-level radiative flux estimates are validated in section 5, followed by the summary discussion.

2. Swath-level surface radiative fluxes

The first component of the NFLUX system, for the radiative heat fluxes, processes satellite swath-level atmospheric profile and surface data into swath-level SW_{dwn} and LW_{dwn} estimates using the Rapid Radiative Transfer Model for Global Circulation Models (RRTMG). The RRTMG (Clough et al. 2005; Iacono et al. 2008; Morcrette et al. 2008), developed by Atmospheric and Environmental Research, Inc. (AER), is based on the line-by-line radiative transfer model and utilizes the correlated-k method (Mlawer et al. 1997) for computational efficiency. The correlated-k method divides the longwave (10–3250 cm^{-1}) and shortwave (850–50 000 cm^{-1}) spectrum into 16 and 14 smaller bands, respectively. A relatively small set of absorption coefficients is then used to represent all frequencies in a given band. The RRTMG longwave version-4.85 and shortwave version-3.9 codes are used in this study and were obtained from the AER RRTM website (http://rtweb.aer.com/rrtm_frame.html).

The primary inputs to both longwave and shortwave RRTMG are atmospheric temperature and moisture profiles. Both longwave and shortwave RRTMG account for clouds, aerosols, and atmospheric gases including ozone (O_3), carbon dioxide (CO_2), methane (CH_4), nitrous oxide (N_2O), and oxygen (O_2). Shortwave RRTMG accounts for atmospheric extinction from Rayleigh scattering. Longwave RRTMG accounts for atmospheric absorption from four halocarbons: chlorofluorocarbon-11 (CFC-11), CFC-12, hydrochlorofluorocarbon-22 (HCFC-22), and carbon tetrachloride (CCl_4). Other inputs that are used within RRTMG include ocean surface albedo, SST, ocean surface emissivity (here set to constant 0.99), and solar constant (here set to constant 1367 $W\,m^{-2}$). Figure 1 from the companion paper (May et al. 2017) shows a simple schematic of the data flow discussed here.

a. Temperature and moisture profiles

Satellite swath-level atmospheric temperature and moisture profiles are obtained from the operational Microwave Integrated Retrieval System (MIRS; Boukabara et al. 2011). MIRS produces atmospheric temperature and moisture profiles at 100 constant pressure layers from 1085 to 0.01 hPa. MIRS is a follow-on and upgrade to the National Environmental Satellite, Data, and Information Service (NESDIS) Microwave Surface and Precipitation

TABLE 1. Satellite platforms and corresponding sensors that are used to produce the operational MIRS products. The satellite LTAN and the footprint resolution (Res) for the MIRS products are also included.

Platform	Sensor(s)	LTAN	Res (km)
DMSP *F16*	SSMIS	1722	45
DMSP *F18*	SSMIS	2006	45
MetOp-A	AMSU-A/MHS	2129	45
MetOp-B	AMSU-A/MHS	2131	15
NOAA-18	AMSU-A/MHS	1523	45
NOAA-19	AMSU-A/MHS	1339	45

Products System (MSPPS). MIRS utilizes an iterative 1D variational inversion scheme that relies on the Community Radiative Transfer Model (CRTM) for the forward and adjoint operators.

The operational MIRS swath-level products are available for six polar-orbiting satellite platforms (Table 1). The MIRS products from the Defense Meteorological Satellite Program (DMSP) *F16* and *F18* platforms use the Special Sensor Microwave Imager/Sounder (SSMIS) sensor. The MIRS products from the European Organisation for the Exploitation of Meteorological Satellites (EUMETSAT) *MetOp-A* and *MetOp-B* platforms and the National Oceanic and Atmospheric Administration (NOAA) *NOAA-18* and *NOAA-19* platforms use the Advanced Microwave Sounding Unit-A (AMSU-A) and the Microwave Humidity Sounder (MHS) sensors. Version 7 netCDF MIRS sounder data, available starting 10 April 2013, were obtained from the NOAA Comprehensive Large Array-Data Stewardship System (CLASS) website (https://www.nsof.class.noaa.gov/saa/products/welcome). MIRS DMSP *F16* products were terminated as of 24 February 2014 because of a sensor data quality issue; however, data prior to the termination are used within NFLUX. The MIRS swath-level data also contain quality control flags and surface type. If the MIRS quality control flag is identified as "bad" or the surface type is not identified as "ocean," surface fluxes are not calculated for that particular swath-level retrieval.

b. Clouds

In addition to the atmospheric temperature and moisture profiles, the MIRS products also provide atmospheric profiles for nonprecipitating clouds, rain, and ice. According to Boukabara et al. (2011), MIRS solves for the surface and atmospheric parameters simultaneously using a two-retrieval-attempt method. In the first attempt, the system assumes a rain-free and ice-free atmosphere. If this retrieval attempt reaches convergence within the CRTM, which is generally 90%–95% of the time, then a nonprecipitating cloud is retrieved and a cloud liquid water (CLW) profile is output. If the first attempt does not reach convergence, then the retrieval is reinitialized and a second retrieval attempt is performed with multiple scattering turned on in the forward model, which allows for convergence in liquid (rain) and frozen (ice) precipitating conditions. If this second attempt reaches convergence, a precipitating cloud is retrieved and a rain water path (RWP) and/or ice water path (IWP) profile is output.

The RRTMG cloud inputs are derived from the MIRS CLW profile data. The RRTMG code used in this study does not include the Monte Carlo Independent Column Approximation (McICA) capability, which would allow representation of subgrid cloud variability such as cloud fraction and cloud overlap. This means that cloud inputs are limited to fully overcast conditions. Assigning a fully overcast cloud to each atmospheric layer that has a nonnegligible CLW value would greatly over represent the cloud coverage in the MIRS data. Therefore, at each MIRS swath-level latitude/longitude, a total CLW value is calculated from the total integrated CLW profile. A single fully overcast cloud, containing the total CLW, is assigned to the atmospheric layer that contains the greatest amount of CLW from the profile. Then, to reduce noise and fill in missing values in the retrievals, an average total CLW at each swath-level latitude/longitude is determined by taking a simple average of the local total CLW value and the eight surrounding total CLW values. The average total CLW is used as the in-cloud water path input to the RRTMG. The cloud water effective radius is set to 10 μm, following the International Satellite Cloud Climatology Project (ISCCP; Rossow and Schiffer 1999). Within RRTMG, optical depths due to water clouds are computed by a method based on the parameterization of water clouds by Hu and Stamnes (1993).

The MIRS RWP and IWP profile data are associated with precipitating clouds. In the presence of atmospheric rain or ice, the moisture profile should not be used since it is unreliable (Boukabara et al. 2011). The RRTMG cannot produce surface fluxes without a moisture profile. Therefore, surface fluxes are not calculated for swath-level locations that contain nonzero RWP and/or IWP profiles.

c. Aerosols

The RRTMG aerosol inputs are derived from the NRL Aerosol Analysis and Prediction System (NAAPS) global gridded fields, which are produced at the Fleet Numerical Meteorology and Oceanography Center (FNMOC) and obtained from the U.S. Naval Oceanographic Office (NAVOCEANO). NAAPS is an operational aerosol forecast model that produces 6-hourly forecast fields of total column aerosol optical depth (AOD) for three aerosol types: smoke, dust, and sulfate (Zhang et al.

2008). Total column AODs are provided for each aerosol type on a constant $1° \times 1°$ global grid for 18 wavelengths, including 0.55 μm. The NAAPS forecast field closest in time to the MIRS retrieval time is horizontally interpolated from the NAAPS global grid to the swath-level latitude–longitude locations. This provides each swath-level latitude–longitude with a spatially interpolated total column smoke, dust, and sulfate AOD for 18 wavelengths.

Shortwave RRTMG uses AOD profiles, separated by aerosol type, at the 0.55-μm wavelength to account for aerosol extinction. The ratio of the average optical thickness in the 14 shortwave RRTMG spectral bands to that at 0.55 μm, as well as the average single scatter albedo and average asymmetry parameter, are determined internally. To make the separate AOD profiles, the NAAPS-provided smoke, dust, and sulfate total column AODs at 0.55 μm are vertically distributed using an exponential decay weighting function based on a given scale height (Zhang et al. 2013; McComiskey et al. 2008). Constant scale heights of 8, 2, and 1 km are used for the smoke, dust, and sulfate types, respectively (Hess et al. 1998).

Longwave RRTMG does not have an internal aerosol parameterization based on a single input channel. Instead, it uses a single combined AOD profile at 16 specific spectral bands, which do not identically match the available NAAPS wavelengths. There are three primary steps to make the required longwave aerosol inputs. The first step interpolates and extrapolates the total column AOD from the given 18 wavelengths in NAAPS to the expected 16 spectral bands in the longwave RRTMG using the Ångström formula for each aerosol type. The spectral dependence of a given AOD (τ_α) can be parameterized with the Ångström exponent (α) using the Ångström formula (Ångström 1929):

$$\tau_\alpha = \beta\lambda^{-\alpha}, \tag{1}$$

where λ is the wavelength in micrometers and β is the optical depth at $\lambda = 1\,\mu$m. The Ångström parameters can then be derived for a given spectral range by applying a linear least squares fit to the Ångström formula (linear fit in a log–log plot of the AOD versus wavelength):

$$\ln\tau_\alpha = -\alpha\ln\lambda + \ln\beta, \tag{2}$$

where the slope of the straight line yields α and the intercept provides β. The Ångström parameters are determined for the given NAAPS spectral range (0.45–12.5 μm) following the ''spectral window method'' (Adeyewa and Balogun 2003; Cachorro et al. 2000, 2001; Kaskaoutis and Kambezidis 2006, 2008). In this method, AODs at strong absorption bands of water vapor and mixed gases are omitted, as they can lead to large uncertainties in AOD. The 8.72–10.14-μm band is a strong absorber of water vapor; therefore, NAAPS data within this interval have been eliminated. The linear least squares fit is applied to the remaining NAAPS wavelengths to obtain the Ångström parameters, which are then used to determine the total column AOD at the midpoint of each of the 16 longwave RRTMG bands, for each aerosol type. The second step produces a vertical profile AOD from the total column AOD for each aerosol type at each of the 16 longwave RRTMG spectral bands. This follows the same method described for the shortwave RRTMG input. The third step produces a single combined AOD profile at each of the 16 longwave RRTMG spectral bands by taking a simple sum of the smoke, dust, and sulfate AOD for each vertical profile layer.

d. Atmospheric gases

Atmospheric gases are input to RRTMG using vertical profiles. The ozone RRTMG input is determined from the daily Stratosphere Monitoring Ozone Blended Analysis (SMOBA) fields produced by the Climate Prediction Center. The daily SMOBA fields contain ozone mixing ratios for 24 vertical levels ranging from 0.2 to 1000 hPa on a constant $2.5° \times 2.5°$ global grid (Yang et al. 2006). SMOBA data were obtained through anonymous FTP (ftp.cpc.ncep.noaa.gov/SMOBA/). To use the SMOBA data as input to the RRTMG, the daily ozone field that matches the MIRS retrieval day undergoes two separate interpolations. First, the daily ozone field is horizontally interpolated from the provided global grid to the swath-level latitude–longitude locations. Then, the spatially interpolated swath-level ozone data are interpolated vertically from the 24 SMOBA vertical levels to match the 100 MIRS pressure levels.

The remaining atmospheric gas concentrations are input to the RRTMG with constant vertical profiles. Oxygen is input with a constant vertical profile of 0.21 mol/mol mixing ratio. The remaining atmospheric gas concentrations are determined for the MIRS retrieval year from the 2013 annual global mean surface mixing ratios and the 2012–2013 annual global mean growth rates reported by the World Meteorological Organization (WMO; Dlugokencky et al. 2014). Mean values for each of the gases are provided in Table 2.

e. Ocean surface albedo

Ocean surface albedo (OSA) is represented in the shortwave RRTMG using direct and diffuse surface reflection components for both the UV–visible and near-IR spectrum ranges. The direct surface albedo component

TABLE 2. RRTMG atmospheric gas concentrations. The inputs are based on the 2013 annual global surface mean and the 2012/13 annual global growth rate. Units are shown in the table as parts per million (ppm), parts per billion (ppb), and parts per trillion (ppt).

Atmospheric gas	2013 annual mean	2012/13 growth rate
CO_2 (ppm)	395.3	2.8
CH_4 (ppb)	1814.1	5.7
N_2O (ppb)	325.9	0.9
CFC-11 (ppt)	234.5	−1.9
CFC-12 (ppt)	521.8	−2.9
HCFC-22 (ppt)	223.6	5.6
CCL_4 (ppt)	84.4	−1.0

corresponds to the direct surface solar radiation, or solar radiation arriving at Earth's surface that traveled in a straight line with the sun's direct beam. The diffuse surface albedo component corresponds to the diffuse surface solar radiation, or solar radiation arriving at Earth's surface after having been scattered by molecules and particles in the atmosphere. The longwave RRTMG does not use OSA.

Direct and diffuse albedo components are determined following the parameterization by Jin et al. (2011). The individual components are calculated as a function of solar zenith angle, ocean surface roughness (wind speed), clear- versus cloudy-sky conditions, and wavelength. There is also a small contribution to OSA from the ocean volume scattering below the surface, which is associated with the chlorophyll concentration and is limited to the visible spectrum (Jin et al. 2011). In this study, this subsurface contribution is ignored. The wind speed used in the parameterizations is set to 6.64 m s^{-1}, the global average 10-m wind speed over the ocean, as determined by Archer and Jacobson (2005). In general, as the solar zenith angle increases (the sun approaches the horizon), the OSA increases. Also, clear skies generally have a higher OSA than cloudy skies. The direct OSA has a typical range of 0.02–0.45, while the diffuse OSA typically ranges from 0.05 to 0.06.

f. Sea surface temperature

The SST input to the RRTMG is obtained from the U.S. Navy Global Ocean Forecasting System (GOFS; Metzger et al. 2014), which consists of the global Hybrid Coordinate Ocean Model (HYCOM) and the Navy Coupled Ocean Data Assimilation (NCODA; Cummings and Smedstad 2013). Global HYCOM is a real-time eddy-resolving global system, with a horizontal equatorial resolution of 1/12.5°. In this application, NCODA uses a three-dimensional variational data assimilation scheme. NCODA is cycled with HYCOM to provide updated initial conditions for subsequent model forecast. GOFS is run daily at the NAVOCEANO to produce 3-hourly forecast fields out to 168 h. The 3-h SST field that is closest in time to the MIRS retrieval time is horizontally interpolated from the provided global grid to the swath-level latitude–longitude locations.

3. Clearness index

In addition to the SW_{dwn} and LW_{dwn} swath-level estimates produced by the RRTMG, NFLUX also produces swath-level clearness index (CI) values corresponding to each SW_{dwn} observation. CI is also called the shortwave atmospheric transmittance (Liou 1992; Petty 2006; Inman et al. 2013; Boilley and Wald 2015) and is defined as the ratio of the irradiance at the surface (SW_{dwn}) to the extraterrestrial irradiance on a horizontal plane, or the incoming solar radiation at the top of atmosphere (SW_{TOA}):

$$\mathrm{CI} = \mathrm{SW}_{\mathrm{dwn}}/\mathrm{SW}_{\mathrm{TOA}}. \tag{3}$$

SW_{TOA} is calculated by

$$\mathrm{SW}_{\mathrm{TOA}} = S_0\left(\frac{r_0}{r}\right)^2 \cos Z, \tag{4}$$

where S_0 is the solar constant, r_0 is the mean sun–Earth distance, r is the instantaneous sun–Earth distance that varies throughout the year according to the elliptical orbit, and Z is the solar zenith angle. CI represents the overall extinction by clouds and atmospheric constituents relative to the incoming solar radiation at the top of atmosphere (Diagne et al. 2013) and can be considered an attenuation factor of the atmosphere. CI values range from 0 to 1. A clear atmosphere (clear-sky conditions, low aerosol contamination, and low water vapor content) would result in a high CI value. A nonclear atmosphere (cloudy-sky conditions, high aerosol contamination, and high water vapor content) would result in a low CI value. CI is a more favorable parameter than SW_{dwn} to use for assimilation across a range of times because CI reduces the dependency on the solar zenith angle.

4. In situ observations

The in situ data used in this study for the radiative flux validation include observations from research vessels and moored buoys (Fig. 1). Research vessels that are part of the Shipboard Automated Meteorological and Oceanographic System (SAMOS) initiative provide SW_{dwn} and LW_{dwn} observations. A SAMOS is an automated datalogging system that records continuous (typically every 1 min) navigational, meteorological, and near-surface oceanographic parameters while the

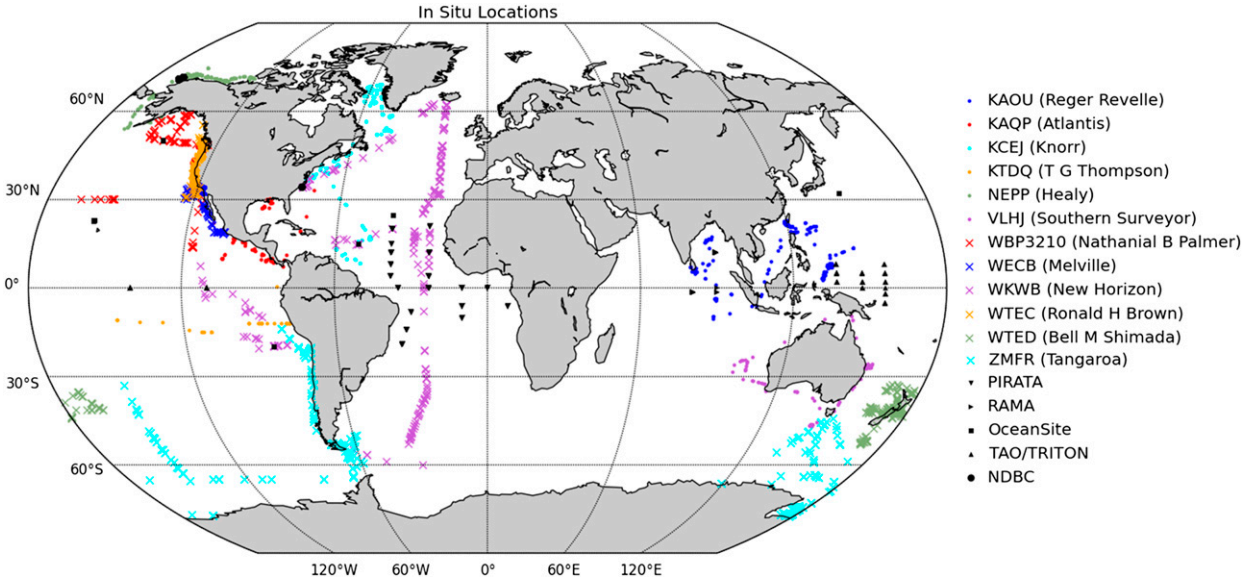

FIG. 1. Locations of in situ validation data. Colored markers represent individual SAMOS ship tracks. The black symbols represent each of the different buoy arrays used.

research vessel is underway (Briggs et al. 2016). When the ship is in port, no measurements are recorded. SAMOS intermediate daily files used in this study were obtained through anonymous FTP (ftp://ftp.coaps.fsu.edu/samos_pub/). A total of 12 SAMOS equipped research vessels provided SW_{dwn} observations for the time period of interest in this study; 9 of the 12 research vessels also provided useful LW_{dwn} observations. One research vessel did not provide LW_{dwn} observations, and two research vessels had a large number of LW_{dwn} observations outside of the normal range which caused us to exclude their LW_{dwn} data from our dataset.

In situ fluxes measured by moored buoys were obtained from five different arrays: Prediction and Research Moored Array in the Tropical Atlantic (PIRATA), Research Moored Array for African–Asian–Australian Monsoon Analysis and Prediction (RAMA), Tropical Atmosphere Ocean/Triangle Trans-Ocean Buoy Network (TAO/TRITON), OceanSites, and National Data Buoy Center (NDBC). PIRATA (Bourlès et al. 2008) provided SW_{dwn} observations from 18 platforms, with 6 of these also providing LW_{dwn} observations. RAMA (McPhaden et al. 2009), located in the Indian Ocean, has 6 platforms that provided SW_{dwn} observations, but none included LW_{dwn} observations for the time period in this study. The tropical Pacific contains the TAO/TRITON (McPhaden et al. 1998), which included 14 platforms with SW_{dwn} observations, 2 of which also provided LW_{dwn} observations. (PIRATA, RAMA, and TAO/TRITON buoy data were obtained from http://www.pmel.noaa.gov/tao/.) NDBC applied a quality control and stored data from three moored buoys with SW_{dwn} observations and none with LW_{dwn} observations. Those with SW_{dwn} observations include station 41036, an NDBC owned and maintained platform that is located off the North Carolina coast, and stations 48213 and 48214, which are owned and maintained by Shell Arctic and located off the northern coast of Alaska. The Alaska stations only operate during summer months. (The NDBC data were obtained from http://www.ndbc.noaa.gov/.) The remaining six moored buoys used in this study are part of the OceanSites network (http://www.oceansites.org/) and provided both SW_{dwn} and LW_{dwn} observations. These moored platforms include the Northwest Tropical Atlantic Station (NTAS) buoy located in the tropical North Atlantic, the Kuroshio Extension Observatory (KEO) buoy located in the western Pacific, the Papa buoy located in the eastern Pacific, the Salinity Processes in the Upper Ocean Regional Study (SPURS) buoy located in the subtropical North Atlantic, the Stratus buoy located in the eastern tropical South Pacific, and the Woods Hole Oceanographic Institution (WHOI) Hawaii Ocean Time Series Station (WHOTS) buoy located in the tropical central Pacific. (KEO and Papa data were obtained from http://www.pmel.noaa.gov/ocs/data/disdel/. NTAS, SPURS, Stratus, and WHOI buoy data were obtained from http://uop.whoi.edu/projects/projects.html.)

As shown in Fig. 1, the different in situ types sample different latitude regions. The NDBC moored buoys are located at high latitudes. The SAMOS research vessels sample the entire latitude range of interest, including cruises to Antarctica, Greenland, and the tropics. The

OceanSites moored buoys also sample a wide range of latitudes. The OceanSites platform Stratus is located at 20°S, while the OceanSites platform Papa is located at 50°N. The PIRATA, RAMA, and TAO/TRITON moored buoys all sample the tropics. By including each of these different in situ types in the NFLUX swath-level comparisons, we hope to ensure evaluation over a wide range of conditions.

All the buoy and research vessel observations in this study use the Eppley Precision Spectral Pyranometer (PSP) to measure the SW_{dwn} and the Eppley Precision Infrared Radiometer (PIR) to measure the LW_{dwn} (Hosom et al. 1995). The reporting frequency of the in situ observations ranges from 1 min to hourly, depending on the platform. Gupta et al. (2004) found that 1-min in situ SW_{dwn} observations are not representative of the cloud spatial variability within a given satellite footprint. To help compensate for the large cloud spatial variability represented in the satellite swath-level data, they found 60-min averaging windows to be the optimum averaging interval for in situ observations under cloudy conditions. The in situ data used in this study do not provide cloud observations; therefore, all in situ SW_{dwn} observations have a 60-min averaging window applied. Gupta et al. (2004) also found averaging the longwave observations resulted in little to no effect on the error statistics because longwave fluxes are much less sensitive to cloud variability than shortwave fluxes. Thus, the in situ LW_{dwn} observations used for validation have no averaging window applied.

5. Swath-level comparisons

The NFLUX swath-level estimates are compared with in situ observations for one year, from 1 May 2013 through 30 April 2014. For a satellite/in situ matchup to be considered valid, the spatial difference between the NFLUX swath-level estimate and the in situ observation must be no more than half of the satellite resolution. The NFLUX swath-level estimates are provided at the same resolution as the MIRS data (Table 1): 15 km for *MetOp-B* and 45 km for the other satellite platforms. Also, the temporal difference between the NFLUX swath-level estimate and the center of the in situ observation averaging window must be within 1 min. There is a slight reduction in the number of DMSP *F16* matchups relative to the other satellites because of the termination of its MIRS product as of 24 February 2014. The calculated values include the satellite mean, mean bias, standard deviation of the difference, root-mean-square error of the difference (RMSE), mean absolute percent error (MAPE), and correlation coefficient. With the exception of MAPE, the error statistics are calculated following May et al. (2016). The mean bias is calculated as NFLUX minus the in situ observations. A positive bias indicates an overestimation of NFLUX, and a negative bias indicates an underestimation of NFLUX. MAPE is a measure of prediction accuracy and is defined using

$$\mathrm{MAPE} = \left(\frac{1}{n}\sum_{i=1}^{n}\left|\frac{X_i - Y_i}{X_i}\right|\right)100, \tag{5}$$

where X_i are the in situ observations and Y_i are the NFLUX estimates. Multiplying by 100 makes it a percent error.

a. Downwelling surface shortwave radiation

The NFLUX swath-level SW_{dwn} error statistics for each satellite versus the in situ observations are presented in Table 3. Corresponding scatterplots are shown in Fig. 2, with different colors representing each of the in situ types. SW_{dwn} is primarily dependent on solar zenith angle and cloud coverage. Because of the dependency on the solar zenith angle, the NFLUX SW_{dwn} mean values for different satellite platforms (third column of Table 3) are highly correlated with the satellite crossing time (Table 1). For example, DMSP *F16* has an early morning local time of the ascending node (LTAN) so the matchups will occur during early morning when there is a relatively low amount of SW_{dwn}. This leads to SW_{dwn} estimates ranging from 25 to 600 W m^{-2} and a low combined matchup mean value of 135.22 W m^{-2}. In contrast, *NOAA-19* has an early afternoon LTAN so the matchups will occur during early afternoon when there is potentially a large amount of SW_{dwn}. This corresponds to SW_{dwn} estimates ranging from 25 to 1100 W m^{-2} and a relatively high combined matchup mean value of 622.65 W m^{-2}. The sampled latitude ranges of the different in situ types also have a large impact on the sample of SW_{dwn} mean values since throughout the year in situ platforms at higher latitudes will not receive as much SW_{dwn} as platforms located in the tropics. This is most easily seen with *NOAA-19*. The high-latitude NFLUX versus NDBC moored buoy matchups have a mean of 195.91 W m^{-2}, while the tropical NFLUX versus TAO/TRITON moored buoy matchups have a mean of 775.24 W m^{-2}. This feature can also be seen in the bottom-right panel of Fig. 2. The tropical moored buoy matchups (warm colors) are clustered between 600 and 1000 W m^{-2}, while the high-latitude NDBC moored buoy matchups (dark blue) are seen typically less than 400 W m^{-2}. The SAMOS research vessel and OceanSites moored buoy matchups (light blue and green), which sample a wide range of latitude, are seen throughout the sampled range.

Bias estimates grouped by in situ type offers insight into the range of conditions sampled. NFLUX SW_{dwn}

TABLE 3. Comparison of the NFLUX swath-level SW_{dwn} estimates with in situ surface observations. Error statistics for each in situ type are shown, as well as a combined type which represents the combination of all six in situ types. The error statistics include number of observations (N), mean bias (Bias), standard deviation (SD), RMSE, MAPE, and correlation coefficient (R^2). Errors are in watts per meter squared.

In situ type	N	Mean	Bias	SD	RMSE	MAPE	R^2
			DMSP *F16*				
SAMOS	282	155.69	1.74	77.45	77.47	52.64	0.78
NDBC	53	146.81	17.69	82.41	84.29	51.62	0.53
OceanSites	312	136.46	−14.89	56.16	58.10	35.75	0.87
PIRATA	426	120.07	5.04	43.46	43.75	32.85	0.81
RAMA	27	158.50	18.68	36.53	41.03	27.81	0.84
TAO/TRITON	65	120.63	−7.77	38.06	38.84	26.12	0.85
Combined	1165	135.22	−0.92	59.18	59.19	38.78	0.81
			DMSP *F18*				
SAMOS	407	266.18	−19.46	99.27	101.16	33.05	0.86
NDBC	128	161.75	−25.72	81.98	85.92	30.41	0.73
OceanSites	339	225.05	−58.25	90.94	108.00	27.65	0.86
PIRATA	711	328.35	10.45	88.15	88.77	26.88	0.74
RAMA	70	366.68	35.96	67.60	76.57	20.11	0.71
TAO/TRITON	112	355.52	1.72	73.91	73.93	19.13	0.76
Combined	1767	285.38	−11.78	93.49	94.23	27.94	0.81
			MetOp-A				
SAMOS	384	416.90	−9.15	127.92	128.25	34.40	0.88
NDBC	95	219.87	−5.87	116.54	116.69	33.94	0.80
OceanSites	367	431.91	−37.93	110.41	116.74	25.19	0.90
PIRATA	718	631.11	23.06	120.50	122.69	18.40	0.65
RAMA	74	661.12	13.59	104.51	105.39	14.83	0.58
TAO/TRITON	107	666.88	−9.00	100.34	100.75	13.47	0.64
Combined	1745	523.15	−0.80	120.47	120.48	23.74	0.86
			MetOp-B				
SAMOS	430	418.27	7.50	122.27	122.50	31.61	0.91
NDBC	127	243.81	20.41	126.84	128.47	49.75	0.64
OceanSites	350	493.44	−6.51	126.39	126.56	23.97	0.86
PIRATA	709	660.15	53.52	122.26	133.46	20.26	0.64
RAMA	58	662.41	44.76	118.47	126.64	20.14	0.57
TAO/TRITON	146	682.49	26.94	127.42	130.23	20.80	0.51
Combined	1820	543.76	26.38	126.06	128.79	25.75	0.86
			NOAA-18				
SAMOS	369	357.46	13.30	108.78	109.59	37.58	0.88
NDBC	91	181.09	16.67	85.39	87.00	41.78	0.87
OceanSites	326	357.71	−3.38	109.32	109.38	34.79	0.86
PIRATA	632	432.46	35.49	97.77	104.01	27.21	0.73
RAMA	53	409.08	−9.09	102.18	102.58	21.37	0.56
TAO/TRITON	126	438.88	−12.16	91.09	91.89	18.93	0.75
Combined	1597	385.28	16.12	103.37	104.62	31.14	0.84
			NOAA-19				
SAMOS	429	512.48	12.11	143.33	143.84	37.20	0.89
NDBC	90	195.91	−18.48	116.76	118.21	43.73	0.69
OceanSites	321	544.83	−33.52	142.21	146.11	23.67	0.86
PIRATA	658	753.01	41.54	154.23	159.73	20.92	0.53
RAMA	65	768.15	16.40	136.63	137.61	15.84	0.43
TAO/TRITON	101	775.24	−16.45	142.48	143.43	16.02	0.42
Combined	1664	622.65	11.73	148.82	149.28	26.38	0.85

estimates relative to OceanSites platforms always have a negative bias, which indicates NFLUX underestimates SW_{dwn} in the mid- to high latitudes. When compared with the PIRATA and RAMA platforms, NFLUX has a positive bias for all satellites except *NOAA-18*. This indicates NFLUX overestimates SW_{dwn} in the tropics. NFLUX relative to the remaining in situ types shows a mix of positive and negative biases for the various satellites, with an overall trend of a positive bias. As discussed previously, incoming solar radiation is largely affected by cloud coverage. Cloudy conditions reduce the amount of solar radiation that reaches the surface, while clear conditions allow most of the incoming solar radiation to reach the surface. The bias results here suggest

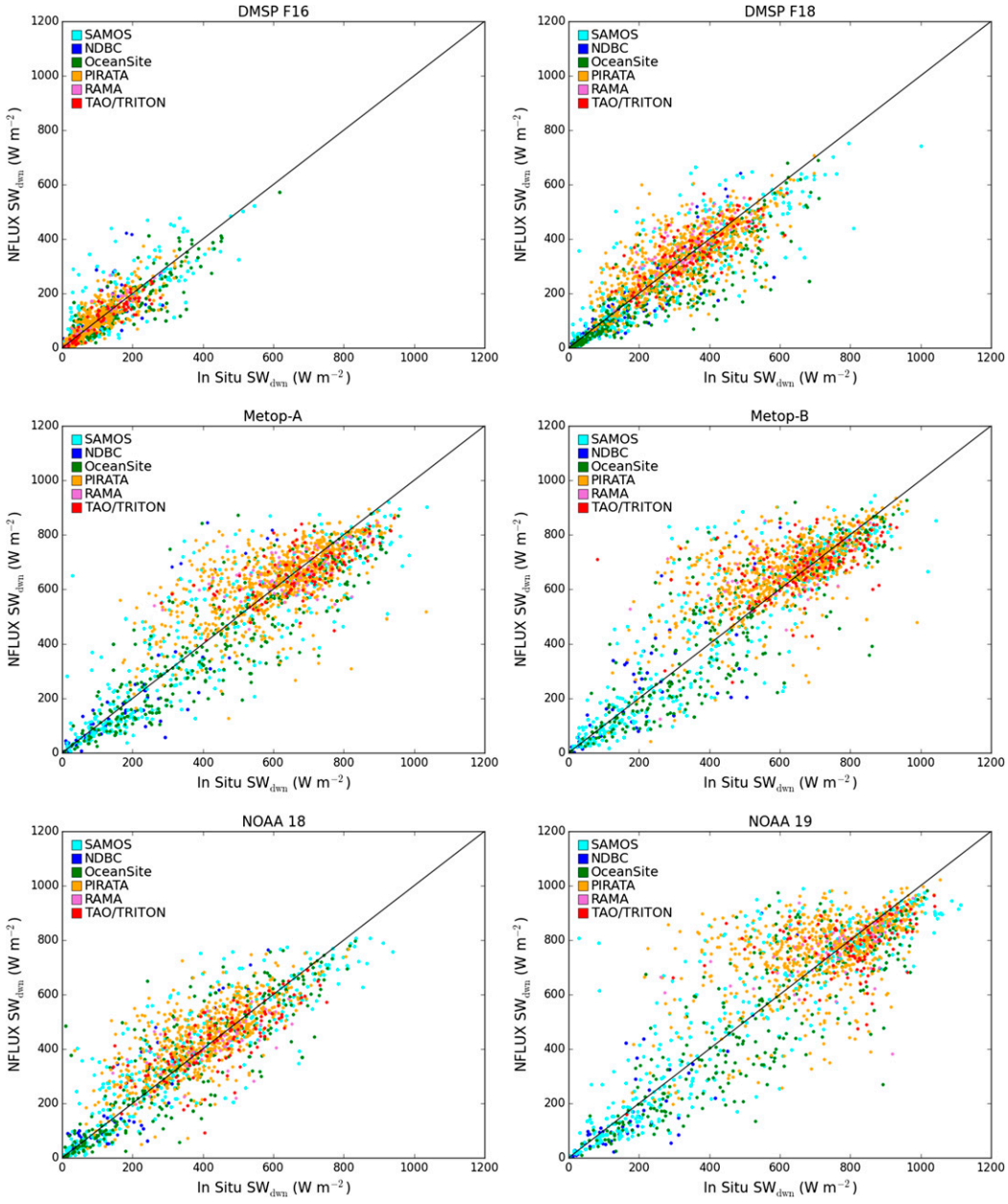

FIG. 2. Graphical comparison of NFLUX vs in situ SW_{dwn} observations for each satellite. Colored markers represent separate in situ data types.

that the MIRS data underestimate cloud coverage in the tropics, causing NFLUX to overestimate SW_{dwn}, and have an overabundance of clouds in the mid- to high latitudes, causing NFLUX to underestimate SW_{dwn}. The underestimation of clouds in the tropics from the MIRS data has also been identified by the MIRS team (C. Grassotti 2016, personal communication). Later versions of the MIRS data, starting with version 11, have increased overall cloud liquid water, particularly in the tropics.

Even with the improvements in MIRS, version 11, some error associated with the cloud coverage is anticipated because MIRS uses a microwave, as opposed to a visible and/or infrared, sensor to retrieve cloud liquid water. Visible and infrared measurements are often used to determine cloud type, cloud thickness, and cloud-top height (Liu et al. 1995). Passive microwave radiation, which can propagate through clouds, is routinely used to provide cloud liquid water paths over the ocean (Weng and Grody 1994; Greenwald et al. 2007; O'Dell et al.

2008; Aires et al. 2011). However, microwave observations are less sensitive to thin clouds than are visible and infrared measurements (O'Dell et al. 2008; Aires et al. 2011). Also, as noted in Boukabara et al. (2011), the MIRS CLW depends on certain assumptions about the clouds, such as the size of the droplets and particle size distribution. By using alternate assumptions in MIRS, the resulting CLW could be different. The particle size has less of an impact on visible and infrared measurements.

The SW_{dwn} standard deviation and RMSE matchup error statistics are difficult to compare among the satellites because they are relative to the sampled range, which largely depends on the LTAN of satellite and the latitude range of the in situ data. As expected, NFLUX SW_{dwn} estimates from DMSP *F16*, with an early morning crossing time, small sampled range, and low combined mean value, have the lowest combined matchup standard deviation and RMSE of 59.18 and 59.19 $W m^{-2}$, respectively. NFLUX SW_{dwn} estimates from *NOAA-19*, with an early afternoon crossing time, large sampled range, and high combined mean value, has the highest combined matchup standard deviation and RMSE of 148.82 and 149.28 $W m^{-2}$, respectively.

As a way to compare the errors in relative terms, corresponding MAPE values are examined. The combined matchup MAPE value for the NFLUX SW_{dwn} estimates from DMSP *F16* has the highest amount of error (38.78%) when compared with the other satellites, which range from 23.74% to 31.14%. The NFLUX SW_{dwn} estimates in comparison with the SAMOS research vessels and the NDBC moored buoys have the largest MAPE values (highest amount of error) for each of the satellites. The NFLUX estimates in comparison with the OceanSites moored buoys generally have the next largest MAPE value, followed by the comparisons with the tropical moored buoys (least amount of error). These results indicate that NFLUX SW_{dwn} estimates compare better to the tropical moored buoys than the other in situ types. Colbo and Weller (2009) identify tilt effects (both mean tilt and rocking tilt caused by surface waves) as the primary source of error for the in situ shortwave radiometer sensors. The shortwave radiometer sensor height is 3–5 m for the moored buoys and 10–20 m for research vessels. From the results seen here, we can speculate there are sampling differences based on platform motion and sensor height.

b. *Clearness index*

The NFLUX swath-level CI error statistics for each satellite versus the in situ observations are presented in Table 4. Corresponding scatterplots are shown in Fig. 3, with each in situ type represented by a separate color. As discussed before and shown in Fig. 2, the NFLUX SW_{dwn} observations have an upper limit based on the satellite LTAN. In contrast, Fig. 3 shows that the NFLUX CI estimates for each satellite sample the entire CI range well, from 0.05 through 0.8. This is because CI is representative of how clear the atmosphere is and is less dependent on the solar zenith angle, which allows for a more direct comparison of values derived from satellites with different LTANs. The combined matchup mean values range from 0.36 to 0.57 for the various satellites. The NFLUX matchups for satellites with early morning LTANs, DMSP *F16* and *F18*, yield lower mean values relative to the matchups with the other satellites. These differences are attributed to the CI calculation not taking into account the atmospheric air mass, the optical pathlength of the atmospheric boundary layer the radiation must travel through to reach ground level (Inman et al. 2013). The airmass coefficient is expressed as a ratio relative to the optical pathlength of the atmospheric boundary layer when the sun is directly overhead. When the sun is directly overhead the airmass coefficient has a value of unity; as the solar zenith angle increases, so does the airmass coefficient. CI does not typically apply a correction for the air mass as commonly used in solar forecasting (Boland 2015; Diagne et al. 2013; Inman et al. 2013).

The NFLUX CI mean bias trends match those discussed for SW_{dwn}. The NFLUX CI estimates relative to PIRATA and RAMA moored buoys always have a positive or neutral bias, which indicates NFLUX overestimates the CI in the tropics. The NFLUX versus OceanSites matchups have a negative bias, which indicates NFLUX underestimates the CI in the mid- to high latitudes. NFLUX versus the remaining in situ types show no consistent trend. An overestimation of CI would suggest the modeled atmosphere is too clear, possibly from lack of clouds or aerosol content. An underestimation of CI would suggest the modeled atmosphere is not clear enough, possibly from too much cloud coverage or aerosol content. As with the SW_{dwn} results, these results suggest MIRS has too few clouds in the tropics and too much cloud coverage in the mid- to high latitudes.

The CI standard deviation and corresponding RMSE matchup values compare well among the various satellites. NFLUX CI estimates from DMSP *F16* have a slightly higher combined standard deviation of 0.17 when compared with NFLUX estimates from other satellites, which range from 0.13 to 0.14. Evaluating the results by in situ type reveals the NFLUX comparisons with NDBC moored buoys have the highest standard deviation and RMSE for the MetOp and NOAA platforms, while the NFLUX comparisons with SAMOS

TABLE 4. As in Table 3, but for CI. Errors are unitless.

In situ type	*N*	Mean	Bias	SD	RMSE	MAPE	R^2
			DMSP *F16*				
SAMOS	327	0.35	−0.02	0.20	0.20	55.91	0.42
NDBC	59	0.33	0.05	0.19	0.19	74.04	0.19
OceanSites	352	0.32	−0.06	0.14	0.15	30.89	0.66
PIRATA	478	0.38	0.00	0.16	0.16	34.91	0.24
RAMA	32	0.40	0.03	0.10	0.10	26.51	0.63
TAO/TRITON	69	0.41	−0.05	0.17	0.18	26.99	0.32
Combined	1317	0.36	−0.02	0.17	0.17	40.18	0.44
			DMSP *F18*				
SAMOS	441	0.41	−0.03	0.15	0.16	35.05	0.69
NDBC	143	0.30	−0.03	0.13	0.13	27.38	0.50
OceanSites	360	0.34	−0.09	0.13	0.16	27.63	0.73
PIRATA	711	0.48	0.02	0.13	0.13	27.00	0.55
RAMA	70	0.55	0.05	0.10	0.11	20.30	0.29
TAO/TRITON	112	0.54	0.00	0.12	0.12	19.13	0.51
Combined	1837	0.43	−0.02	0.14	0.14	28.35	0.66
			MetOp-A				
SAMOS	402	0.46	−0.01	0.15	0.15	35.34	0.76
NDBC	116	0.32	−0.04	0.18	0.19	30.39	0.41
OceanSites	369	0.46	−0.04	0.12	0.13	24.99	0.81
PIRATA	718	0.60	0.02	0.11	0.12	18.42	0.54
RAMA	74	0.64	0.01	0.10	0.10	14.87	0.37
TAO/TRITON	107	0.65	−0.01	0.10	0.10	13.47	0.39
Combined	1786	0.53	−0.01	0.13	0.13	23.92	0.74
			MetOp-B				
SAMOS	436	0.48	0.01	0.14	0.14	28.64	0.80
NDBC	136	0.41	0.05	0.20	0.21	52.59	0.34
OceanSites	354	0.52	−0.01	0.14	0.14	23.71	0.77
PIRATA	709	0.63	0.05	0.12	0.13	20.33	0.52
RAMA	58	0.64	0.04	0.11	0.12	20.19	0.50
TAO/TRITON	146	0.66	0.02	0.12	0.13	20.70	0.26
Combined	1839	0.56	0.03	0.14	0.14	25.36	0.72
			NOAA-18				
SAMOS	399	0.47	0.01	0.16	0.16	37.23	0.73
NDBC	99	0.34	0.01	0.18	0.18	45.36	0.41
OceanSites	350	0.45	−0.01	0.15	0.15	28.41	0.74
PIRATA	632	0.56	0.04	0.13	0.13	27.06	0.50
RAMA	53	0.55	−0.01	0.13	0.13	21.34	0.11
TAO/TRITON	126	0.58	−0.01	0.13	0.13	19.24	0.42
Combined	1659	0.50	0.02	0.14	0.15	30.11	0.68
			NOAA-19				
SAMOS	439	0.52	0.01	0.15	0.15	35.63	0.79
NDBC	101	0.32	−0.03	0.17	0.17	39.37	0.52
OceanSites	321	0.52	−0.04	0.14	0.14	23.70	0.77
PIRATA	658	0.64	0.03	0.13	0.14	20.88	0.44
RAMA	65	0.65	0.02	0.12	0.12	15.80	0.25
TAO/TRITON	101	0.67	−0.01	0.12	0.12	15.91	0.36
Combined	1685	0.57	0.01	0.14	0.14	25.88	0.73

research vessels have the highest standard deviation and RMSE for the DMSP platforms. The other in situ types, the tropical and the OceanSites moored buoys, show good agreement to NFLUX with similar standard deviation and RMSE values for the various satellites. The corresponding MAPE values reinforce these findings. The NFLUX comparisons with the NDBC moored buoys and the SAMOS research vessels have the highest MAPE values for each of the satellites, indicating that NFLUX has the largest amount of error relative to these two in situ types, consistent with the SW_{dwn} results. The NFLUX CI estimates derived from DMSP *F16* have the largest combined matchup MAPE value of 40.18%, while the combined matchup MAPE value for NFLUX using the other satellites ranges from 23.92% to 30.11%. This indicates that the NFLUX estimates based on the

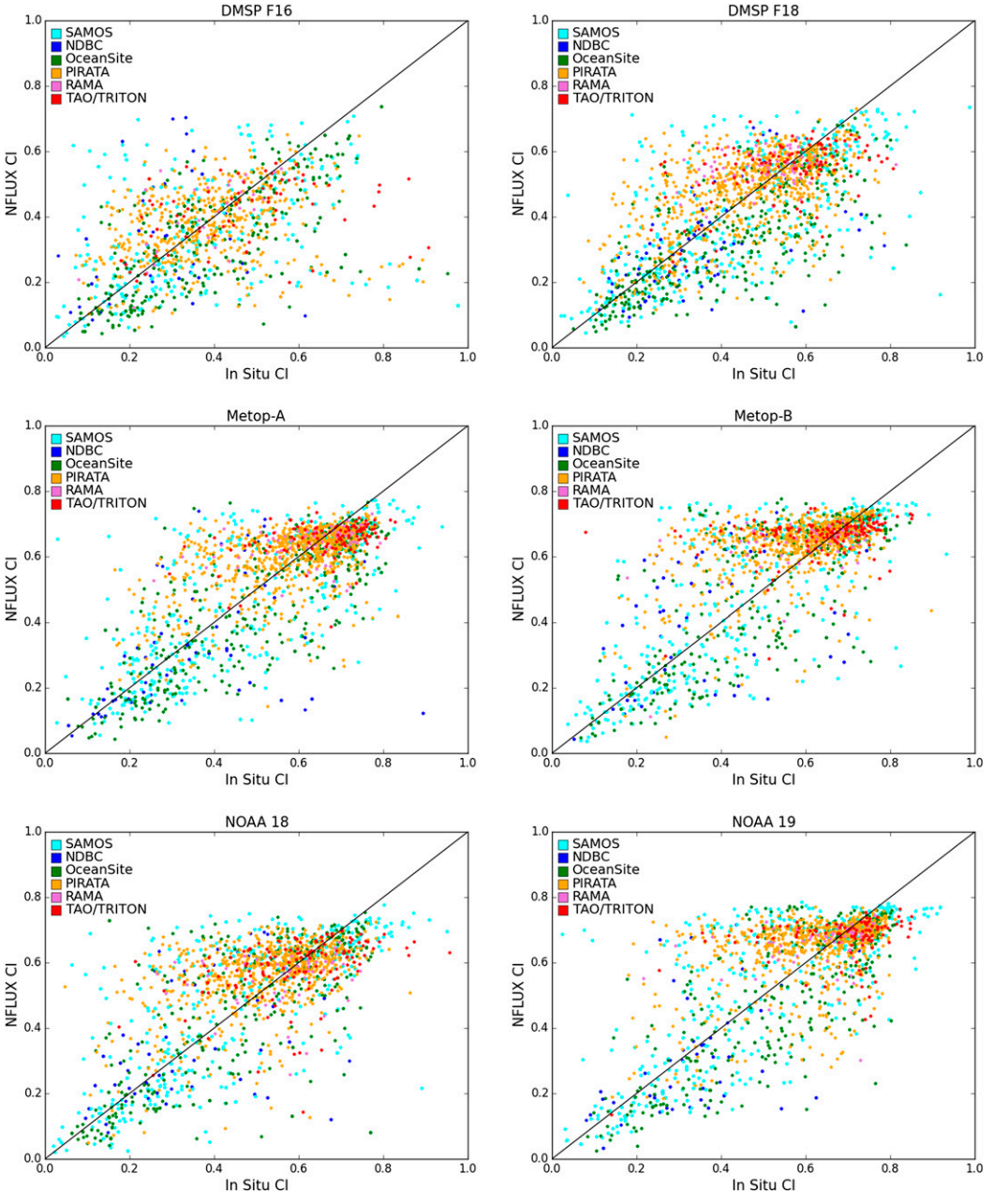

FIG. 3. As in Fig. 2, but for CI.

DMSP *F16* satellite have larger errors than do estimates from the other satellites.

The correlation coefficient of the NFLUX CI estimates shows a noticeable difference between DMSP *F16* and the other satellites. The NFLUX estimates from DMSP *F16* have a combined matchup correlation coefficient of 0.44, while the combined matchups from the other satellites range from 0.66 to 0.74. This indicates a good agreement between the in situ observations and NFLUX among the DMSP *F18*, MetOp, and NOAA satellites.

c. *Downwelling surface longwave radiation*

The NFLUX swath-level LW_{dwn} error statistics for each satellite versus the in situ observations are presented in Table 5. Figure 4 shows the corresponding scatterplots, with different colors representing each of the separate in situ types. The NDBC and RAMA moored buoys did not provide high-resolution LW_{dwn} observations during this time period, so these in situ types are not included in Table 5 or Fig. 4. We also note

TABLE 5. As in Table 3, but for LW_{dwn}. Errors are in watts per meter squared.

In situ type	*N*	Mean	Bias	SD	RMSE	MAPE	R^2
			DMSP *F16*				
SAMOS	378	356.51	−1.11	25.39	25.41	5.73	0.84
OceanSites	688	372.97	−2.50	22.22	22.36	4.54	0.79
PIRATA	514	394.95	−5.77	18.43	19.32	3.59	0.56
TAO/TRITON	106	390.81	1.56	20.33	20.39	3.85	0.49
Combined	1686	377.10	−2.93	21.91	22.11	4.47	0.81
			DMSP *F18*				
SAMOS	631	362.08	7.32	25.91	26.92	6.34	0.86
OceanSites	762	365.25	4.90	20.88	21.45	4.74	0.89
PIRATA	706	405.85	−1.94	15.89	16.00	2.96	0.54
TAO/TRITON	49	399.11	10.35	16.73	19.67	4.29	0.61
Combined	2148	378.43	3.49	21.38	21.66	4.61	0.89
			MetOp-A				
SAMOS	728	360.11	0.80	22.40	22.42	5.01	0.89
OceanSites	981	369.85	0.41	19.48	19.48	4.02	0.88
PIRATA	931	405.72	−1.27	14.50	14.55	2.77	0.60
TAO/TRITON	87	396.66	13.88	16.91	21.87	5.09	0.51
Combined	2727	380.35	0.37	18.92	18.93	3.89	0.90
			MetOp-B				
SAMOS	863	355.10	−4.45	22.31	22.75	4.92	0.89
OceanSites	1012	361.86	−6.11	19.33	20.27	4.06	0.88
PIRATA	995	399.04	−7.58	14.01	15.93	2.82	0.64
TAO/TRITON	90	389.44	3.85	14.63	15.13	3.31	0.79
Combined	2960	373.23	−5.82	18.70	19.59	3.87	0.90
			NOAA-18				
SAMOS	778	359.66	−0.89	23.97	23.99	5.29	0.86
OceanSites	909	366.03	−1.51	20.70	20.75	4.43	0.87
PIRATA	807	403.97	−3.89	15.31	15.80	2.88	0.62
TAO/TRITON	74	394.45	6.94	15.15	16.67	3.40	0.71
Combined	2568	376.84	−1.83	20.25	20.33	4.17	0.88
			NOAA-19				
SAMOS	835	354.30	−0.27	23.88	23.88	5.38	0.88
OceanSites	980	364.99	−0.78	20.11	20.12	4.23	0.88
PIRATA	871	402.34	−6.93	15.09	16.61	2.96	0.62
TAO/TRITON	63	391.61	9.14	15.82	18.27	3.77	0.68
Combined	2749	374.18	−2.35	20.18	20.31	4.16	0.89

the higher number of observations relative to the SW_{dwn} and CI comparisons, because LW_{dwn} matchups can occur during both daytime and nighttime. Unlike SW_{dwn}, LW_{dwn} does not depend on solar zenith angle, so the satellite LTAN has no impact on the NFLUX LW_{dwn} estimates. The latitude range of the in situ data does have an impact on the LW_{dwn} matchup mean values. As discussed previously, LW_{dwn} has a large dependency on low-level atmospheric temperature, which is correlated with latitude. This effect can be seen from the NFLUX mean values in Table 5 (third column). The NFLUX LW_{dwn} estimates in comparison with the SAMOS research vessels and OceanSites moored buoy observations, which sample the given latitude range, have significantly lower mean values (354.30–372.97 W m^{-2}) than the NFLUX versus PIRATA and TAO/TRITON moored buoy matchups (389.44–405.85 W m^{-2}), which are limited to the tropical region. This effect is also reflected in the scatterplots in Fig. 4. The tropical moored buoy matchups (orange and red) are seen typically above 350 W m^{-2}, while the matchups for the other in situ types (blue and green) are spread throughout the sampled range. The NFLUX mean value for each in situ type is similar among the various satellites, which reemphasizes that LW_{dwn} does not depend on the solar zenith angle. This also leads to the combined mean matchup values being close among the various satellites, ranging from 373.23 to 380.35 W m^{-2}.

The NFLUX LW_{dwn} estimates relative to the TAO/TRITON moored buoy observations always have a positive bias, which indicates NFLUX overestimates LW_{dwn} in the tropical Pacific. The NFLUX versus PIRATA moored buoy matchups always have a negative bias, which indicates NFLUX underestimates LW_{dwn} in the tropical Atlantic. The NFLUX estimates in comparison

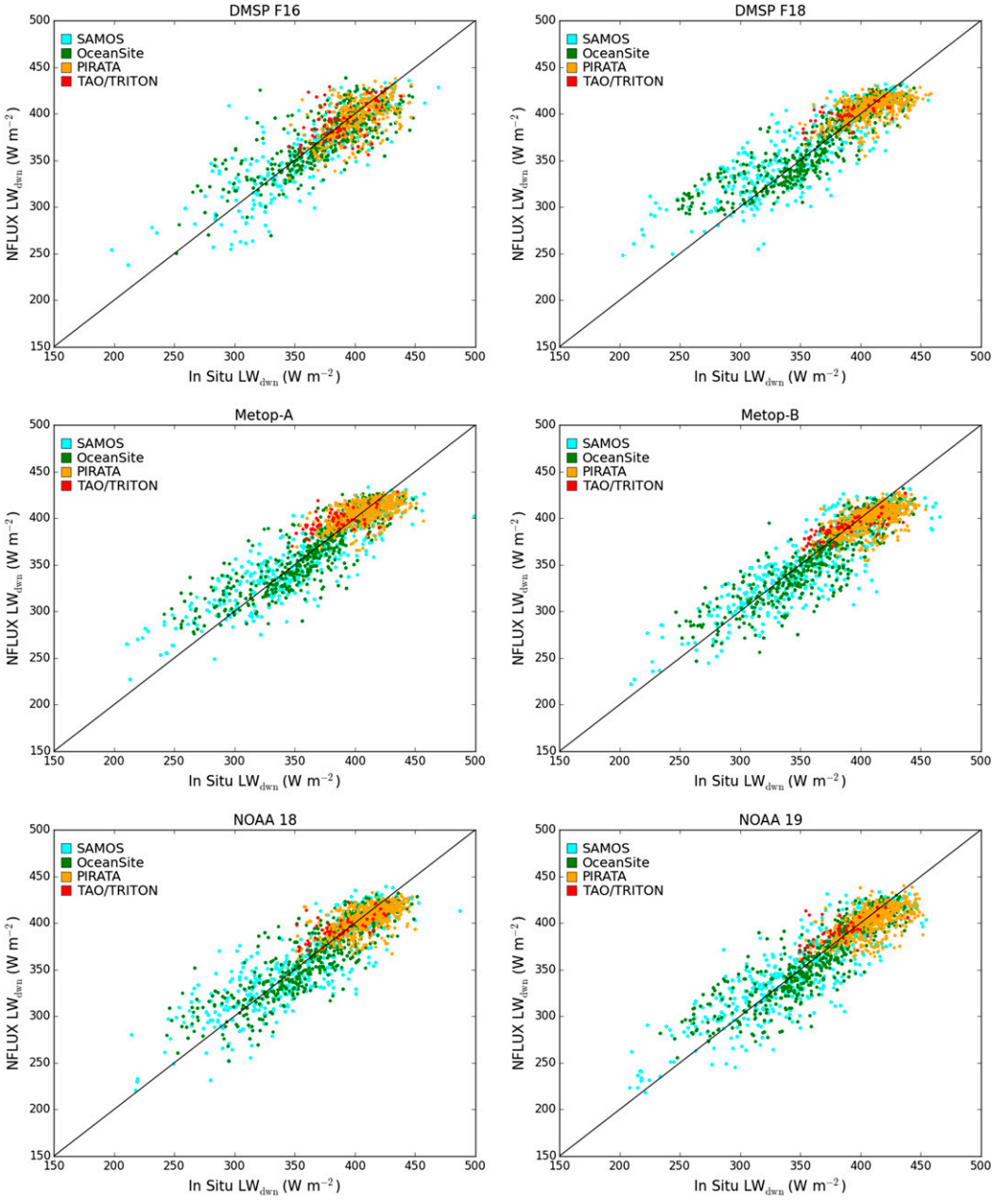

FIG. 4. As in Fig. 2, but for LW_{dwn}.

with SAMOS research vessels and OceanSites moored buoy observations also have a negative bias for all satellite products except DMSP *F18* and *MetOp-A*. LW_{dwn} is largely influenced by the low-level atmospheric temperature and moisture. Warm and moist conditions increase LW_{dwn}, while cool and dry conditions reduce LW_{dwn}. The biases here suggest that the MIRS data are too warm or moist in the tropical Pacific, causing NFLUX to overestimate LW_{dwn}, and too cool or dry in other regions, causing NFLUX to underestimate LW_{dwn}.

The LW_{dwn} standard deviation and RMSE matchup values compare well among the various satellite, with the standard deviation for the combined matchups ranging from 18.70 to 21.91 W m^{-2} and the corresponding RMSE values ranging from 18.93 to 22.11 W m^{-2} for the various satellites. Comparisons of NFLUX with the SAMOS research vessels always show a slightly higher standard deviation and RMSE relative to comparisons with the other in situ types for each satellite. Additionally, matchups relative to the SAMOS research vessels have slightly larger

MAPE values, ranging from 4.92% to 6.34%, than do matchups with other in situ types, with MAPE values ranging from 2.77% to 5.09%. Colbo and Weller (2009) found that the most significant error for the in situ longwave radiometer sensors is from thermal gradients in the dome and case temperatures due to differential heating. This will affect the instantaneous measurements, which is what is used in this study, but typically has little to no effect on the long-term averages. Dome contamination from the accumulation of salt spray or other opaque materials on the radiometer dome can also affect the measurements. The combined matchup MAPE values range from 3.87% to 4.61% for the various satellites, with those using the DMSP satellites showing slightly larger MAPE values than do the MetOp and NOAA satellites. The matchups with the SAMOS research vessels and the OceanSites moored buoys generally show larger correlation coefficients than do the matchups with the PIRATA and TAO/TRITON moored buoys. The combined correlation coefficients range from 0.88 to 0.90, with the exception of DMSP *F16*, which has a combined correlation coefficient of 0.81. In general, these results imply a good agreement between the in situ observations and the NFLUX estimates among the various satellites.

To further examine the LW_{dwn} results, the combined matchups were separated by day and night for each satellite (not shown). The distribution of the matchups was very similar and there was no significant difference between the error characteristics.

6. Summary and conclusions

The goal of the NFLUX project is to provide near-real-time global gridded surface heat flux products. This study discusses the production and evaluation of the satellite-based swath-level radiative heat fluxes. The RRTMG is used to provide swath-level SW_{dwn} and LW_{dwn} estimates. The primary input to the RRTMG is MIRS data, which are available for six different satellite platforms. Using multiple satellites with a variety of sampling times provides global coverage of radiative flux estimates throughout the day, which is required for accurate ocean model forecasting. The swath-level SW_{dwn} estimates are converted into CI values. By definition, CI is SW_{dwn} normalized by SW_{TOA}. CI can be used as a measure of how clear the atmosphere is. The NFLUX SW_{dwn}, CI, and LW_{dwn} swath-level estimates are evaluated relative to a variety of in situ observations from research vessels and 5 moored buoy arrays for one year, May 2013–April 2014.

The NFLUX swath-level SW_{dwn} and CI estimates have a positive bias in the tropics, indicating an overestimation by NFLUX, and a negative bias in the mid- to high latitudes, indicating an underestimation by NFLUX. These biases are likely due to misrepresentation of cloud coverage by the MIRS data. An increase in cloud coverage would reduce SW_{dwn}, while a decrease in cloud coverage would increase SW_{dwn}. Overall cloud liquid water has been increased in later versions of the MIRS data. The NFLUX swath-level LW_{dwn} estimates have a positive bias in the tropical Pacific, indicating an overestimation by NFLUX, and a negative bias in other regions, indicating an underestimation by NFLUX. The low-level atmospheric temperature and moisture are likely the cause of these biases. Increasing (reducing) the low-level air temperature or moisture increases (reduces) LW_{dwn}.

The NFLUX products from DMSP *F16* have slightly larger errors than do the other satellites for SW_{dwn}, CI, and LW_{dwn}. The remaining five satellite products compare well to each other for each parameter. The SW_{dwn} combined matchup standard deviation ranges from 59.18 to 148.82 $W\,m^{-2}$. This large range is primarily due to the different LTANs for each satellite. The corresponding combined matchup correlation coefficient ranges from 0.81 to 0.86. The CI combined matchup standard deviation ranges from 0.13 to 0.17, and the combined correlation coefficient ranges from 0.44 to 0.74. The LW_{dwn} combined matchup standard deviation ranges from 18.70 to 21.91 $W\,m^{-2}$ and the combined matchup correlation coefficient ranges from 0.81 to 0.90.

These results are very encouraging, but the satellite swath-level estimates are only the first part to the NFLUX system. A companion paper (May et al. 2017) discusses assimilating the swath-level estimates with atmospheric model data to produce global gridded radiative heat flux fields. The NFLUX surface heat flux fields can then be used as an alternative to NWP products to force ocean models. We are also currently working on utilizing NFLUX as a mechanism for using satellite observations of the air–sea interface to assess and monitor NWP products and coupled models.

Acknowledgments. The authors thank L. Zhao for helpful discussions of the MIRS products. This research is funded by the Office of Naval Research Program Element 62435N under the ''Calibration of Ocean Forcing with Satellite Flux Estimates'' Naval Research Laboratory project.

REFERENCES

Adeyewa, Z. D., and E. E. Balogun, 2003: Wavelength dependence of aerosol optical depth and the fit of the Ångström law. *Theor. Appl. Climatol.*, **74**, 105–122, doi:10.1007/s00704-002-0707-3.

Aires, F., F. Marquisseau, C. Prigent, and G. Sèze, 2011: A land and ocean microwave cloud classification algorithm derived from AMSU-A and -B, trained using MSG-SEVIRI infrared and

visible observations. *Mon. Wea. Rev.*, **139**, 2347–2366, doi:10.1175/MWR-D-10-05012.1.

Ångström, A., 1929: On the atmospheric transmission of sun radiation and on dust in the air. *Geogr. Ann.*, **11**, 156–166.

Archer, C. L., and M. Z. Jacobson, 2005: Evaluation of global wind power. *J. Geophys. Res.*, **110**, D12110, doi:10.1029/2004JD005462.

Boilley, A., and L. Wald, 2015: Comparison between meteorological re-analyses from ERA-Interim and MERRA and measurements of daily solar irradiation at surface. *Renewable Energy*, **75**, 135–143, doi:10.1016/j.renene.2014.09.042.

Boland, J., 2015: Spatial-temporal forecasting of solar radiation. *Renewable Energy*, **75**, 607–616, doi:10.1016/j.renene.2014.10.035.

Boukabara, S.-A., and Coauthors, 2011: MiRS: An all-weather 1DVAR satellite data assimilation and retrieval system. *IEEE Trans. Geosci. Remote Sens.*, **49**, 3249–3272, doi:10.1109/TGRS.2011.2158438.

Bourlès, B., and Coauthors, 2008: The PIRATA program: History, accomplishments, and future directions. *Bull. Amer. Meteor. Soc.*, **89**, 1111–1125, doi:10.1175/2008BAMS2462.1.

Briggs, K., S. R. Smith, and J. J. Rolph, 2016: 2015 SAMOS data quality report. COAPS, Tallahassee, FL, 222 pp. [Available online at http://samos.coaps.fsu.edu/html/docs/2015SAMOSAnnualReport_final.pdf.]

Cachorro, V. E., P. Durán, R. Vergaz, and A. M. de Frutos, 2000: Measurements of the atmospheric turbidity of the north-centre continental area in Spain: Spectral aerosol optical depth and Ångström turbidity parameters. *J. Aerosol Sci.*, **31**, 687–702, doi:10.1016/S0021-8502(99)00552-2.

——, R. Vergaz, and A. M. de Frutos, 2001: A quantitative comparison of α-Å turbidity parameter retrieved in different spectral ranges based on spectroradiometer solar radiation measurements. *Atmos. Environ.*, **35**, 5117–5124, doi:10.1016/S1352-2310(01)00321-1.

Clough, S. A., M. W. Shephard, E. J. Mlawer, J. S. Delamere, M. J. Iacono, K. Cady-Pereira, S. Boukabara, and P. D. Brown, 2005: Atmospheric radiative transfer modeling: A summary of the AER codes. *J. Quant. Spectrosc. Radiat. Transfer*, **91**, 233–244, doi:10.1016/j.jqsrt.2004.05.058.

Colbo, K., and R. A. Weller, 2009: Accuracy of the IMET sensor package in the subtropics. *J. Atmos. Oceanic Technol.*, **26**, 1867–1890, doi:10.1175/2009JTECHO667.1.

Cummings, J. A., and O. M. Smedstad, 2013: Variational data assimilation for the global ocean. *Data Assimilation for Atmospheric, Oceanic and Hydrologic Applications*, S. K. Park and L. Xu, Eds., Vol. II, Springer-Verlag, 303–343, doi:10.1007/978-3-642-35088-7_13.

Diagne, M., M. David, P. Lauret, J. Boland, and N. Schmutz, 2013: Review of solar irradiance forecasting methods and a proposition for small-scale insular grids. *Renewable Sustainable Energy Rev.*, **27**, 65–76, doi:10.1016/j.rser.2013.06.042.

Dlugokencky, E. J., B. D. Hall, S. A. Montzka, G. Dutton, J. Muhle, and J. W. Elkins, 2014: Long-lived greenhouse gases [in "State of the Climate in 2013"]. *Bull. Amer. Meteor. Soc.*, **95** (7), S33–S35.

Greenwald, T. J., T. S. L'Ecuyer, and S. A. Christopher, 2007: Evaluating specific error characteristics of microwave-derived cloud liquid water products. *Geophys. Res. Lett.*, **34**, L22807, doi:10.1029/2007GL031180.

Gupta, S. K., D. P. Kratz, A. C. Wilber, and L. C. Nguyen, 2004: Validation of parameterized algorithms used to derive TRMM-CERES surface radiative fluxes. *J. Atmos. Oceanic Technol.*, **21**, 742–752, doi:10.1175/1520-0426(2004)021<0742:VOPAUT>2.0.CO;2.

Hess, M., P. Koepke, and I. Schult, 1998: Optical properties of aerosols and clouds: The software package OPAC. *Bull. Amer. Meteor. Soc.*, **79**, 831–844, doi:10.1175/1520-0477(1998)079<0831:OPOAAC>2.0.CO;2.

Hosom, D. S., R. A. Weller, R. E. Payne, and K. E. Prada, 1995: The IMET (improved meteorology) ship and buoy systems. *J. Atmos. Oceanic Technol.*, **12**, 527–540, doi:10.1175/1520-0426(1995)012<0527:TIMSAB>2.0.CO;2.

Hu, Y. X., and K. Stamnes, 1993: An accurate parameterization of the radiative properties of water clouds suitable for use in climate models. *J. Climate*, **6**, 728–742, doi:10.1175/1520-0442(1993)006<0728:AAPOTR>2.0.CO;2.

Iacono, M. J., J. S. Delamere, E. J. Mlawer, M. W. Shephard, S. A. Clough, and W. D. Collins, 2008: Radiative forcing by long-lived greenhouse gases: Calculations with the AER radiative transfer models. *J. Geophys. Res.*, **113**, D13103, doi:10.1029/2008JD009944.

Inman, R. H., H. T. C. Pedro, and C. F. M. Coimbra, 2013: Solar forecasting methods for renewable energy integration. *Prog. Energy Combust. Sci.*, **39**, 535–576, doi:10.1016/j.pecs.2013.06.002.

Jin, Z., Y. Qiao, Y. Wang, Y. Fang, and W. Yi, 2011: A new parameterization of spectral and broadband ocean surface albedo. *Opt. Express*, **19**, 26 429–26 443, doi:10.1364/OE.19.026429.

Jourdan, D., and C. Gautier, 1995: Comparison between global latent heat flux computed from multisensor (SSM/I and AVHRR) and from in situ data. *J. Atmos. Oceanic Technol.*, **12**, 46–72, doi:10.1175/1520-0426(1995)012<0046:CBGLHF>2.0.CO;2.

Kaskaoutis, D. G., and H. D. Kambezidis, 2006: Investigation into the wavelength dependence of the aerosol optical depth in the Athens area. *Quart. J. Roy. Meteor. Soc.*, **132**, 2217–2234, doi:10.1256/qj.05.183.

——, and ——, 2008: Comparison of the Ångström parameters retrieval in different spectral ranges with the use of different techniques. *Meteor. Atmos. Phys.*, **99**, 233–246, doi:10.1007/s00703-007-0279-y.

Kratz, D. P., S. K. Gupta, A. C. Wilber, and V. E. Sothcott, 2010: Validation of the CERES edition 2B surface-only flux algorithms. *J. Appl. Meteor. Climatol.*, **49**, 164–180, doi:10.1175/2009JAMC2246.1.

——, P. W. Stackhouse, S. K. Gupta, A. C. Wilber, P. Sawaengphokhai, and G. R. McGarragh, 2014: The Fast Longwave and Shortwave Flux (FLASHFlux) data product: Single scanner footprint fluxes. *J. Appl. Meteor. Climatol.*, **53**, 1059–1079, doi:10.1175/JAMC-D-13-061.1.

Liou, K. N., 1992: *Radiation and Cloud Processes in the Atmosphere.* Oxford University Press, 504 pp.

Liu, G., J. A. Curry, and R.-S. Sheu, 1995: Classification of clouds over the western equatorial Pacific Ocean using combined infrared and microwave satellite data. *J. Geophys. Res.*, **100**, 13 811–13 826, doi:10.1029/95JD00823.

May, J. C., C. Rowley, and N. Van de Voorde, 2016: The Naval Research Laboratory ocean surface flux (NFLUX) system: Satellite-based turbulent heat flux products. *J. Appl. Meteor. Climatol.*, **55**, 1221–1237, doi:10.1175/JAMC-D-15-0187.1.

——, ——, and C. Barron, 2017: NFLUX satellite-based surface radiative heat fluxes. Part II: Gridded products. *J. Appl. Meteor. Climatol.*, **56**, 1043–1057, doi:10.1175/JAMC-D-16-0283.1.

McComiskey, A., S. E. Schwartz, B. Schmid, H. Guan, E. R. Lewis, P. Ricchiazzi, and J. A. Ogren, 2008: Direct aerosol forcing: Calculation from observables and sensitivities to inputs. *J. Geophys. Res.*, **113**, D09202, doi:10.1029/2007JD009170.

McPhaden, M. J., and Coauthors, 1998: The Tropical Ocean-Global Atmosphere observing system: A decade of progress. *J. Geophys. Res.*, **103**, 14 169–14 240, doi:10.1029/97JC02906.

——, and Coauthors, 2009: RAMA: The Research Moored Array for African–Asian–Australian Monsoon Analysis and Prediction. *Bull. Amer. Meteor. Soc.*, **90**, 459–480, doi:10.1175/2008BAMS2608.1.

Metzger, E. J., and Coauthors, 2014: US Navy operational global ocean and Arctic ice prediction systems. *Oceanography*, **27**, 32–43, doi:10.5670/oceanog.2014.66.

Mlawer, E. J., S. J. Taubman, P. D. Brown, M. J. Iacono, and S. A. Clough, 1997: Radiative transfer for inhomogeneous atmospheres: RRTM, a validated correlated-*k* model for the longwave. *J. Geophys. Res.*, **102**, 16 663–16 682, doi:10.1029/97JD00237.

Morcrette, J.-J., H. W. Barker, J. N. S. Cole, M. J. Iacono, and R. Pincus, 2008: Impact of a new radiation package, McRad, in the ECMWF Integrated Forecast System. *Mon. Wea. Rev.*, **136**, 4773–4798, doi:10.1175/2008MWR2363.1.

O'Dell, C. W., F. J. Wentz, and R. Bennartz, 2008: Cloud liquid water path from satellite-based passive microwave observations: A new climatology over the global oceans. *J. Climate*, **21**, 1721–1739, doi:10.1175/2007JCLI1958.1.

Petty, G. W., 2006: *A First Course in Atmospheric Radiation*. 2nd ed. Sundog Publishing, 458 pp.

Rossow, W. B., and R. A. Schiffer, 1999: Advances in understanding clouds from ISCCP. *Bull. Amer. Meteor. Soc.*, **80**, 2261–2287, doi:10.1175/1520-0477(1999)080<2261:AIUCFI>2.0.CO;2.

Trenberth, K. E., J. T. Fasullo, and J. Kiehl, 2009: Earth's global energy budget. *Bull. Amer. Meteor. Soc.*, **90**, 311–324, doi:10.1175/2008BAMS2634.1.

Van de Voorde, N., J. May, and C. Rowley, 2015: NFLUX PRE: Validation of new specific humidity, surface air temperature, and wind speed algorithms for ascending/descending directions and clear or cloudy conditions. NRL Rep. NRL/MR/7320–15-9611, 30 pp. [Available online at https://www7320.nrlssc.navy.mil/pubs/2015/may-2015.pdf.]

Wang, D., L. Zeng, X. Li, and P. Shi, 2013: Validation of satellite-derived daily latent heat flux over the South China Sea, compared with observations and five products. *J. Atmos. Oceanic Technol.*, **30**, 1820–1832, doi:10.1175/JTECH-D-12-00153.1.

Weng, F., and N. C. Grody, 1994: Retrieval of cloud liquid water using the Special Sensor Microwave Imager (SSM/I). *J. Geophys. Res.*, **99**, 25 535–25 551, doi:10.1029/94JD02304.

Yang, S.-K., S. Zhou, and A. J. Miller, 2006: SMOBA: A 3-dimensional daily ozone analysis using SBUV/2 and TOVS measurements. NOAA/NWS/Climate Prediction Center. [Available online at http://www.cpc.ncep.noaa.gov/products/stratosphere/SMOBA/smoba_doc.shtml.]

Yu, L., and R. A. Weller, 2007: Objectively analyzed air–sea heat fluxes for the global ice-free oceans (1981–2005). *Bull. Amer. Meteor. Soc.*, **88**, 527–539, doi:10.1175/BAMS-88-4-527.

Zeng, X., M. Zhao, and R. E. Dickinson, 1998: Intercomparison of bulk aerodynamic algorithms for the computation of sea surface fluxes using TOGA COARE and TAO data. *J. Climate*, **11**, 2628–2644, doi:10.1175/1520-0442(1998)011<2628:IOBAAF>2.0.CO;2.

Zhang, J., J. S. Reid, D. L. Westphal, N. L. Baker, and E. J. Hyer, 2008: A system for operational aerosol optical depth data assimilation over global oceans. *J. Geophys. Res.*, **113**, D10208, doi:10.1029/2007JD009065.

Zhang, L., Q. B. Li, Y. Gu, K. N. Liou, and B. Meland, 2013: Dust vertical profile impact on global radiative forcing estimation using a coupled chemical-transport–radiative-transfer model. *Atmos. Chem. Phys.*, **13**, 7097–7114, doi:10.5194/acp-13-7097-2013.

Zhang, Y. C., W. B. Rossow, and A. A. Lacis, 1995: Calculation of surface and top of atmosphere radiative fluxes from physical quantities based on ISCCP data sets: 1. Method and sensitivity to input data uncertainties. *J. Geophys. Res.*, **100**, 1149–1165, doi:10.1029/94JD02747.

——, ——, and P. W. Stackhouse, 2006: Comparison of different global information sources used in surface radiative flux calculation: Radiative properties of the near-surface atmosphere. *J. Geophys. Res.*, **111**, D13106, doi:10.1029/2005JD006873.